Geochemical Perspectives Letters

Pore water chemical constraints on petrophysical shifts following biosilica diagenesis

S. Varkouhi[1*], N.J. Tosca[2], J.A. Cartwright[1], Z. Guo[3], P. Kianoush[4], A. Jurkowska[5]

OPEN ACCESS

https://doi.org/10.7185/geochemlet.2440

Abstract

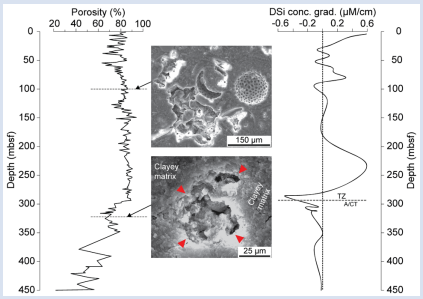

Silica diagenesis commonly induces marked petrophysical changes to biosiliceous sediments across the sub-seafloor opal-A to opal-CT transition zone ($TZ_{A/CT}$). Integration of pore water thermodynamics with textural and mineralogical data reveals that sediments in the $TZ_{A/CT}$ drilled at ODP Site 794 are sharply compacted *via* opal-A dissolution and matrix collapse. The porosity decline is linked to silica solubility through pore water saturation states with opal-A and opal-CT. A dissolved silicon (DSi) drop near the depth of the petrophysical shift implies that fluid expulsion removes the DSi produced by opal-A dissolution. Production of opal-CT from the pore fluid that is thermodynamically equilibrated with solubility of this silica mineral phase however slightly impacts the anomalous compaction at the $TZ_{A/CT}$.

Received 10 June 2024 | Accepted 3 October 2024 | Published 30 October 2024

Introduction

Conventional perspectives on the compaction of deep water deposits deal with petrophysical properties (*e.g.*, porosity, density, and compressional velocity) as gently evolving traits with depth (Wrona *et al.*, 2017a). Nevertheless, siliceous hemipelagic sediments penetrated during the Deep Sea Drilling Project (DSDP) and Ocean Drilling Program (ODP) have undergone pronounced physical property variations (anomalous compaction) that typically accompany biogenic silica (opal-A) alteration toward opal-CT (α-cristobalite/α-tridymite; Varkouhi *et al.*, 2020a). These petrophysical shifts occur through an early burial dissolution-redeposition process whose development is primarily regulated by temperature and time, with lesser controls from siliceous surface area, host lithofacies, and interstitial water chemistry (Williams *et al.*, 1985). Prominent opal-A content reductions ascribed to its dissolution, and the subsequent opal-CT precipitation compact the sediment framework and impose a porosity drop on the host lithology (Wrona *et al.*, 2017b). Distinct sediment density increases occur as porosity declines because pore volume decreases compress the solid matrix by densifying its constituents (Volpi *et al.*, 2003).

The drastic changes in petrophysics of opal-A deposits commonly generate a discrete reflector mainly identifiable on seismic sections when it cross cuts the neighbouring strata (Davies and Cartwright, 2002). This profound reflection marks the position of a transition zone, across which biosilica appreciably dissolves and is replaced with opal-CT ($TZ_{A/CT}$; Varkouhi *et al.*, 2020a). The narrow (≤50 m thick) $TZ_{A/CT}$ hosts both opal-A and opal-CT, whilst the latter phase dominates (Varkouhi *et al.*, 2021). Investigations into silica diagenesis and $TZ_{A/CT}$ characterisation in sub-seabed sediments have been built upon 2D and 3D seismic stratigraphy, scientific drillings, and on-land surveys (Varkouhi *et al.*, 2022). Integration of these procedures with interstitial water chemistry has been applied to the current thermochemical state of biosilica diagenesis across the anomalous compaction section, *i.e.* active *versus* fossilised $TZ_{A/CT}$ (Varkouhi *et al.*, 2020b). Following the original works on oxygen isotope relations among opaline polymorphs involved in silica diagenesis (Knauth and Epstein, 1976; Murata *et al.*, 1977; Pisciotto *et al.*, 1992), Yanchinila *et al.* (2020, 2021) and Ibarra *et al.* (2022) provided constraints on temperatures of biosilica transformation into opal-CT in deep water cherts using high resolution characterisation of oxygen-18 isotopic compositions. The alteration of opal-A to diagenetic opal (opal-CT) ceases in fossilised transitions, signifying that the $TZ_{A/CT}$ is not at the phase predominance boundary between these silica polymorphs (Neagu *et al.*, 2010). Biosilica diagenesis progresses through an active $TZ_{A/CT}$ instead. The view of an active silica diagenesis reaction front is based on the assumption that the $TZ_{A/CT}$ has a regional sea bottom simulating geometry, which cross cuts the nearby stratigraphy, and is likely to be presently advancing upwards (Varkouhi *et al.*, 2022).

1. Department of Earth Sciences, University of Oxford, Oxford OX1 3AN, United Kingdom
2. Department of Earth Sciences, University of Cambridge, Cambridge CB2 3EQ, United Kingdom
3. School of Geographical Sciences, Hebei Normal University, Shijiazhuang 050024, China
4. Department of Petroleum and Mining Engineering, South Tehran Branch, Islamic Azad University, Tehran 1777613651, Iran
5. Faculty of Geology, Geophysics and Environmental Protection, AGH University of Krakow, Krakow 30-059, Poland
* Corresponding author (email: varkouhi1973@gmail.com)

Despite research on the $TZ_{A/CT}$ structure and thermodynamics (*e.g.*, Davies and Cartwright, 2002; Varkouhi *et al.*, 2020b), the silica dissolution/precipitation kinetics driving petrophysical contrasts between porous opal-A deposits and more condensed opal-CT units is poorly understood. While Varkouhi *et al.* (2020b) describe diagenetic states of the $TZ_{A/CT}$ using pore fluid chemical proxies, controls from pore water thermodynamics and kinetic modes of ion transport on petrophysics during silica diagenesis are inconclusive in their work. Elucidating the anomalous compaction drivers is crucial to understanding structural/thermal evolution in basin fills, and plays a role in petroleum systems as the $TZ_{A/CT}$ contributes to drilling risks by often comprising hard cherts (Neagu *et al.*, 2010).

This manuscript aims to link the sudden compaction of deep marine biosiliceous deposits that have undergone silica diagenesis to processes that transport dissolved phases in pore water through this reaction. To fulfil this objective, signatures of variations in interstitial water composition are combined with records of physical property changes and textural, mineralogical, and oxygen isotopic features of sediments subjected to biosilica diagenesis in Site 794 of the ODP Leg 127, the Japan Sea (Fig. S-1a–c). Interstitial water chemical constraints, including saturation states with silica polymorphs and dissolved silicon (DSi) and major ions concentration gradients indicate that opal-A transformation is active over the $TZ_{A/CT}$ in this site and other borehole sites drilling the same transition zone (Varkouhi *et al.*, 2020b). The pore fluid chemical variations can map the position of opal-A removal by dissolution and the resultant petrophysical shifts, pointing to where the diagenetic reaction remains active as diffusion is too slow to erase these chemical signals.

Materials and Methods

Essential data for this work come from the results of interstitial water analyses (Fig. S-2) and physical property measurements for Site 794 available through the International Ocean Discovery Program (IODP) database. Complementary mineralogical, textural, and chemical constraints were furnished with analyses of cored samples from this site. Optical petrography was conducted on smear slides with a Leica DM750 P microscope to describe the sediment biogenic and lithogenic components. Abundances of opal-CT were determined from X-ray diffraction (XRD) scans acquired using a PANalytical Empyrean diffractometer. The software Match! 3.16 identified the crystalline phases and determined their abundance in the sediments. The Reference Intensity Ratio (RIR) method, which scales diffraction data to the diffraction of reference material (corundum), was employed to quantify crystalline components in the samples with multiple phases. Distribution of frustules in the sediment, their dissolution and re-precipitation as opal-CT, and fabric evolution were characterised under a FEI Quanta 650 scanning electron microscope (SEM). Palaeo-temperatures of sediments with precipitated opal-CT were derived from $\delta^{18}O$ values to trace opal-A inversion toward opal-CT through the anomalously compacted sediment interval. The operating procedures for these methods are detailed in the Supplementary Information.

Mineralogical and Textural Make-Up

Biosilica, mainly diatoms, is the sole major biogenic component, while clay-sized materials constitute the leading siliciclastic component of the sediment sequence in Site 794 (Fig. S-3a–e, b–h). The relative extent of opal-A assessed using visual

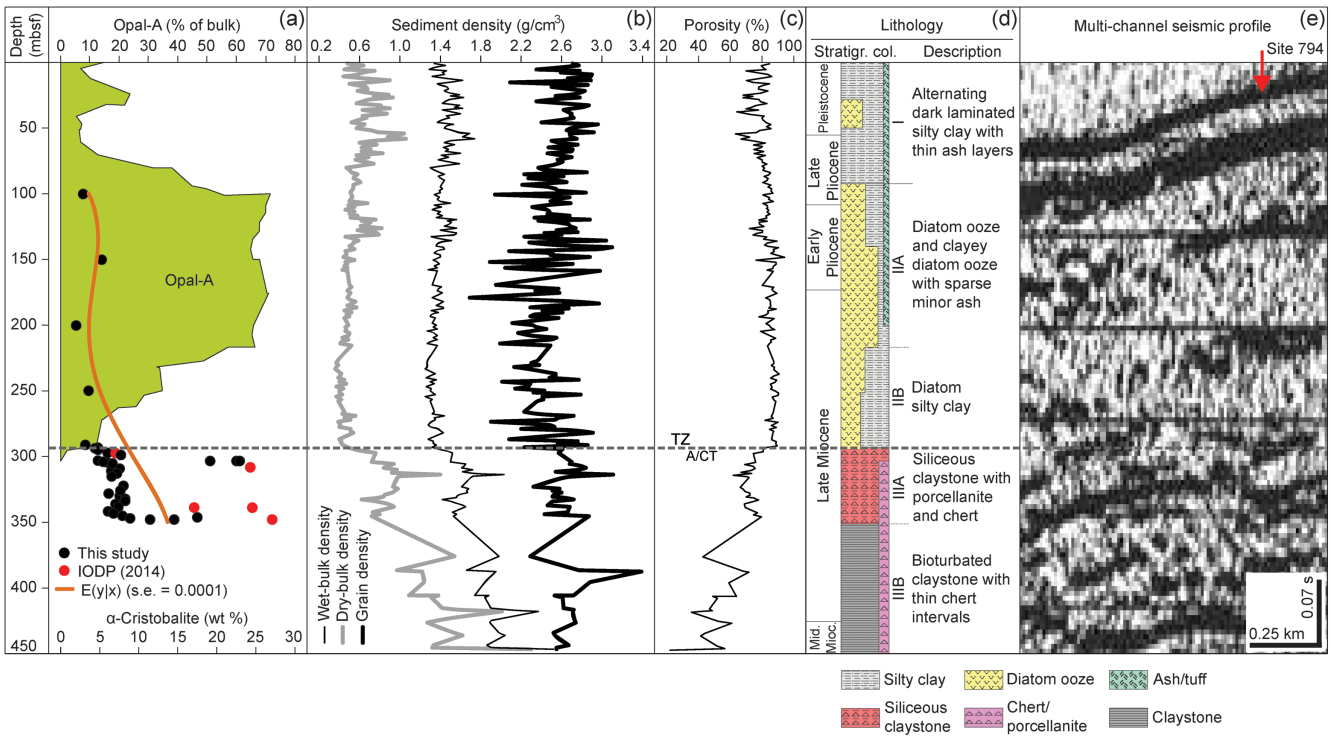

Figure 1 Integration of mineralogical and petrophysical measurements with seismic profiling, Site 794. **(a)** Reduced biosilica extents (green area) correlated with rising opal-CT contents (black and red circles), **(b,c)** anomalous density and porosity changes, and **(d)** onset of chert/porcellanite production across the $TZ_{A/CT}$ at ~293.5 mbsf are tied to **(e)** exhibition of a high amplitude reflector ~0.37 s below the seafloor. The petrophysical profiles were modified from IODP (2014), and the biosilica distribution pattern with depth from Varkouhi *et al.* (2020a, 2020b). E(y|x)—non-linear regression, s.e.—standard error, Mid. Mioc.—middle Miocene, Stratigr. col.—stratigraphic column.

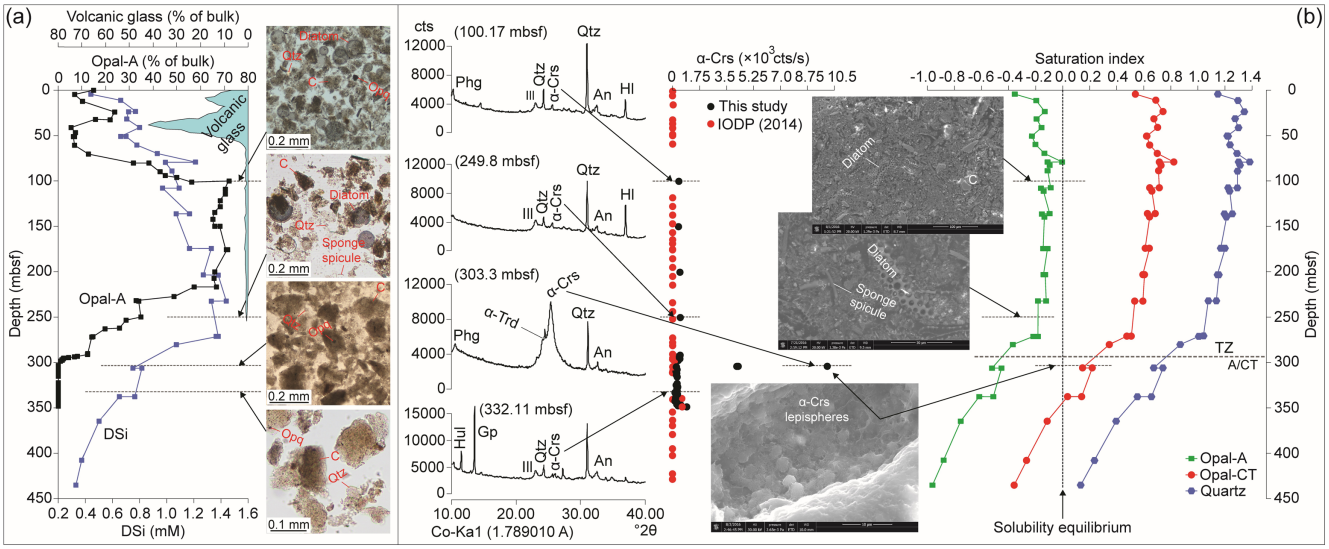

Figure 2 Pore water signatures of silica diagenesis at Site 794. **(a)** DSi profile closely corresponds to opal-A spatial distribution, and **(b)** pore water undersaturation with biosilica but supersaturation with diagenetic opal, and sediment textural evolution (detailed by cristobalite diffraction intensities and photomicrographs). Refer to Table S-1 for the sample identification. The saturation profiles were modified from Varkouhi *et al.* (2020b). The volcanic glass depth profile was based upon IODP (2014) smear slide data. α-Crs—α-cristobalite, α-Trd—α-tridymite, An—anorthite, C—clay, Gp—gypsum, Hl—halite, Hul—heulandite, Ill—illite, Opq—opaque, Phg—phengite, Qtz—quartz.

estimation scheme of Marsaglia *et al.* (2013) records a peak of 72 % at ~100 mbsf for a diatom ooze, mixed with fine volcanic glass, sealing the $TZ_{A/CT}$ reflector of petrophysical changes (Figs. 1a–e, 2a and S-3a). The clayey fraction averaged at ~58 % in the opal-A sediment reaches 93 % within the opal-CT pile. The relative abundance of opal-CT was identified by peak intensities of planar spacing (d) (101) α-cristobalite at 26.18–25.14° 2θ and d(110) α-tridymite grid at 23.98° 2θ in the XRD record of erratically aligned bulk samples (Fig. 2b). The XRD peaks of clayey and fine volcanic materials in multi-phase sediments overprint the diffraction signs of biosilica; making opal-A undetectable using this process. The intensity-depth profile of α-cristobalite as the opal-CT proxy (Damby *et al.*, 2014) displays the initial formation of this phase in the sequence over the $TZ_{A/CT}$ as a weak intensity diffraction set, while its intensity in the $TZ_{A/CT}$ largely varies between 0 and 10260 cts/s (Fig. 2b). The XRD detected normalised quantities of α-cristobalite vary between ~2 and ~27 wt. % and from 3.5 to ~31 wt. % for α-tridymite, with a mean value rise in the opal-CT-rich section to nearly three times that of the opal-A unit (Table S-1). The percentage of anorthite drops when shifting from the opal-A succession to the $TZ_{A/CT}$, but the mean quartz and phengite contents in the opal-CT pile remain close to that of the opal-A section. The siliceous textures in Site 794 exhibit a change in diatom content of the sediment with depth from significant to none (Fig. S-4a–h). The siliceous frustules are largely fragmented and dissolved even at shallow burial depths (Figs. 2a,b, S-4a), and their dissolution degree varies from moderately dissolved (for depths near the seabed) to low close to the base of opal-A interval (Fig. S-4b–e). The microfabric within the $TZ_{A/CT}$ and its underlying unit is featured by rather perfect biosilica dissolution and its replacement by growth of opal-CT lepispheres in a condensed clayey matrix with a reduced porosity (Fig. S-4f–h).

Ionic Transport Modes in Biogenic Silica Diagenesis

Biogenic silica diagenesis in Site 794 has crucially governed the pore water chemistry, particularly the gradient of major ions (Figs. 2a, 3 and S-2). Notable DSi and lithium releases to the interstitial water above, and removal from the pore solution in the $TZ_{A/CT}$, imply that this transition behaves as a diffuse boundary that develops concentration gradients downwards below it and upwards into the ocean water (Varkouhi *et al.*, 2020b; Figs. 2a, S-2). Because the sediment diffusivity changes with burial (Fig. 3), the profiles linking ionic concentrations above and below the $TZ_{A/CT}$ are non-linear. The burial depth reliance of diffusivity is expressed by its connection to pore structures (Yong *et al.*, 2014), indicating the more reduced diffusion in lower porosity opal-CT sediments than in biosiliceous deposits (Fig. 3).

The exceedingly low permeability of biosiliceous deposits (5.35×10^{-20} to 1.97×10^{-14} m^2; Holler, 1992) contributes to their greatly lowered sediment diffusivity with depth, especially in the $TZ_{A/CT}$ and deeper deposits at Site 794 (Fig. 3). Consequently, diffusive flows are negligible drivers for DSi removal from the pore water and bypassing of opal-CT documented across the $TZ_{A/CT}$ (Figs. 1a, 2a,b).

Conversely, a water content depletion coincident with the porosity shifts from biosilica oozes to opal-CT sediments (Fig. 3) supports the argument that DSi and other ions have not diffused in the sediment at rates comparable to those by advective ion transport modes. The opal-CT-rich sediment is thus more compacted than opal-A deposits because its transformation from biosilica involves pore volume reduction when pore water is expelled. The low permeable overburden sealing the $TZ_{A/CT}$ may impede the interstitial fluid expulsion because advection depends on higher permeability rather than diffusive fluxes (Kwon *et al.*, 2004). However, the pore fluid release when opal-A converts into opal-CT is influenced by over pressure, and the low permeability biosilica section above the $TZ_{A/CT}$ allows elevation and perpetuation of the over pressure that drives fluid outfluxes (Davies *et al.*, 2008).

Thermodynamic Indications of Active Silica Diagenesis

The ongoing opal-CT production is evident from highly undersaturated pore water state with biosilica while supersaturated with diagenetic silica polymorphs, including opal-CT and quartz along

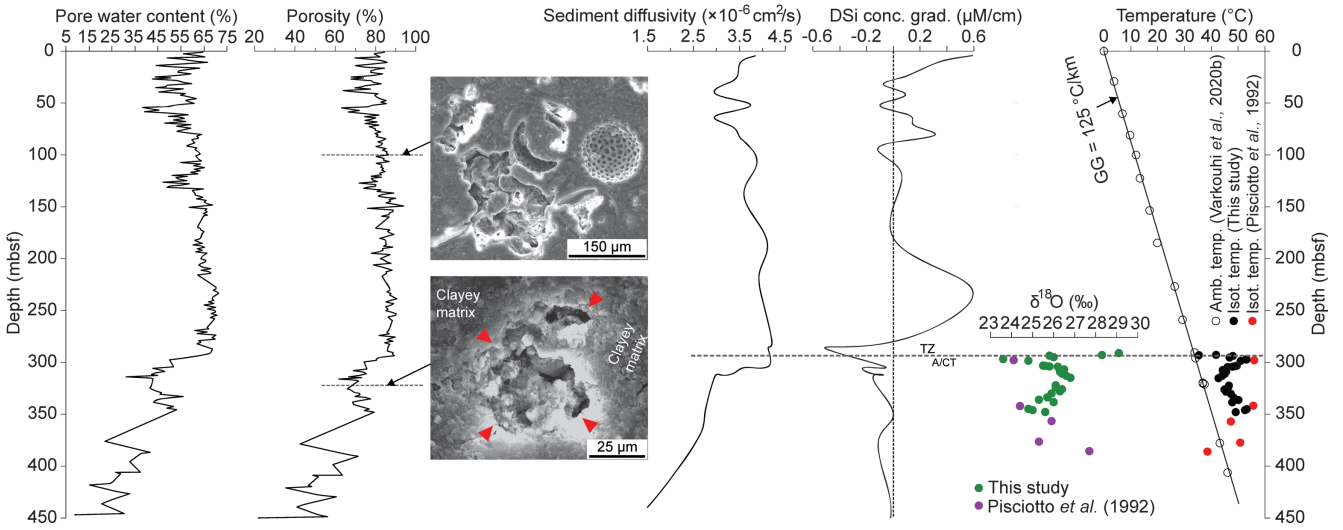

Figure 3 Pore volume drop due to sediment framework compactional collapse (red arrows) *via* pore water expulsion, documented by shifts in DSi gradient, oxygen isotopic composition, and temperatures of the $TZ_{A/CT}$ sediment; Site 794. The inverse DSi gradient indicates its removal, while highly reduced diffusivities occur, at the $TZ_{A/CT}$. The physical property profiles were modified from IODP (2014). The DSi gradient was estimated as concentration differences through each pore water sampling interval, and the sediment diffusivity as $\Phi^2 \times D$, where Φ is the porosity and D (5.5×10^{-6} cm^2/s; Dixit and Van Cappellen, 2003) the free solution silica diffusivity. The $\delta^{18}O$ values used to assess the isotopic temperature of opal-CT (see Table S-2) were computed by following Kita *et al.* (1985). Amb. temp.—ambient temperature, conc. grad.—concentration gradient, GG—geothermal gradient, Isot. temp.—isotopic temperature.

the sediment unit and the $TZ_{A/CT}$ in Site 794 (Figs. 1a, 2b). Consequently, biosilica dissolves throughout the sediment section, but synchronously the opal-CT supersaturated pore fluid in the biosiliceous unit reaches solubility equilibrium with this phase in the $TZ_{A/CT}$ (Fig. 2b). The solubility control is thus reached with opal-CT and yet this polymorph precipitates across the $TZ_{A/CT}$, where it has been largely produced since the late Miocene onset of the transition advancement (Varkouhi *et al.*, 2021).

This further argues for dominance of pore fluid advection with minor influences from diffusion across the interval of significant opal-CT production. The $TZ_{A/CT}$ coincides with the depth of DSi sink, where aqueous DSi leaves the pore water system through huge volumes of the interstitial water expelled, and thus a porosity decrease (Figs. 2a, 3). Co-occurrence of the DSi sink, the sharp physical property variations, and marked opal-CT production in Site 794 $TZ_{A/CT}$ (Figs. 1a–c, 2a,b) demonstrates that this DSi drop is essentially governed by active biosilica diagenesis. Under slow hemipelagic sedimentation (1–104 m/Myr; Varkouhi *et al.*, 2021), advection and diffusion potentially erase signatures of non-steady state DSi concentration drops unless diagenesis still continues or occurred recently (the 10–50 m/Myr accumulation rate in Site 794 falls within slow rate ranges; Shipboard Scientific Party, 1990). If solubility equilibrium with opal-CT and its production had ceased at Site 794, the late Miocene chemical signals of the last phase of silica diagenesis would have been erased in the present concentration profile under advective or even highly reduced diffusive rates.

The solubility equilibration at the boundary of diagenetic silica formation from dissolved opal-A conforms to temperature increases with depth as the assessment of saturation state involves temperature constraints. Hence, opal-CT equilibrates with the pore water as temperature increases with burial, highly suggesting that active opal-CT production in Site 794 links to the present day thermal gradient (Fig. 3).

Clustering of isotopic temperatures for the $TZ_{A/CT}$ sediment section and its underlying unit, extracted from the opal-CT $\delta^{18}O$ using the fractionation relation of Kita *et al.* (1985), near the present temperatures (Fig. 3, Table S-2) supports the notion that biosilica diagenesis has thermodynamically equilibrated with the modern thermal gradient at Site 794 (Pisciotto *et al.*, 1992). Accordingly, the lack of signatures of sudden $\delta^{18}O$ changes with depth in the opal-CT-rich interval, *i.e.* a ~5.5 ‰ range of $\delta^{18}O$ variations maintained throughout the section (Fig. 3), implies that diagenetic opal has acquired these $\delta^{18}O$ records *via* equilibrium with its solubility in the pore water; an indication for the presently active state of the Site 794 $TZ_{A/CT}$.

Anomalous Compaction in Biosilica Deposits - A Synoptic Model

The chemical transition from biosilica to opal-CT concomitant with a porosity drop of ~15 % (from ~80 to ~65 %; Fig. 1c) in the $TZ_{A/CT}$ at Site 794 is closely analogous to those formerly approximated for hemipelagic oozes from geographically diverse basins. For instance, biosilica diagenesis has led to 16 % pore volume reduction in the early Miocene sediment of Norwegian Sea (Shipboard Scientific Party, 1987) and 15 % in the Neogene claystones of New Jersey Atlantic continental slope (Shipboard Scientific Party, 1994). The porosity decline due to opal-A dissolution and consumption underlined here and in comparable works corresponds with other petrophysical shifts, *e.g.*, density and velocity increases and pore water release (Figs. 1b, 3). The association of these petrophysical contrasts with silica diagenetic transformation is described by a conceptual model shown in Figure 4.

Following our model, under oxygen depleted conditions, the pore water DSi extent has been continuously fed by dissolution of biosilica buried below the seabed. Despite low sedimentation rates in Site 794, elevated primary productivity has been able to sustain a continuous opal-A rain to the seabed, and hence is proportional to biosilica burial and DSi recycling (von Breymann *et al.*, 1992). The volcaniclastics (*e.g.*, volcanic glass) admixed with biosilica may impart DSi to the pore fluid in quantities near those of opal-A dissolution. The low volcaniclastic content of the biosilica sequence and its negligible distribution in the $TZ_{A/CT}$ however, display notably less DSi release to the

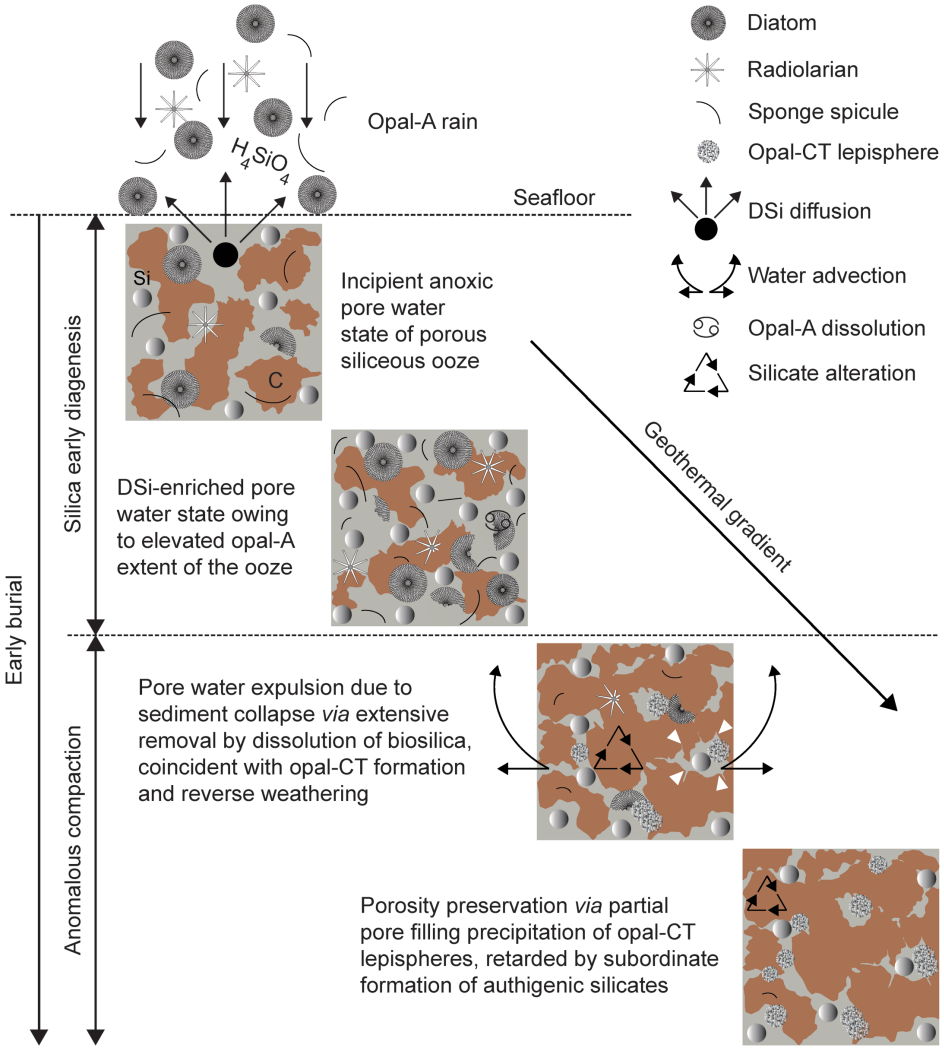

Figure 4 Compactional degradation of biosilica to opal-CT in hemipelagic deposits investigated. Silica diagenesis begins chemically near the seabed, but is not expressed as petrophysical changes until the reaction develops through opal-A dissolution and the removal of DSi by vertical/lateral pore water escape. Opal-CT production, retarded by reverse weathering, partially affects the porosity.

pore solution through volcanic glass alteration than biosilica dissolution (Fig. 2a; Varkouhi *et al.*, 2020b).

The increasing DSi level with depth in the siliceous ooze implies the onset of biosilica early diagenesis (Fig. 2a), but is not expressed as pore fluid expulsion and porosity decreases until the reaction is complete *via* pore water DSi removal and subordinate opal-CT formation (Fig. 4). The anomalous compressional changes when opal-A undergoes appreciable dissolution happen abruptly (Wrona *et al.*, 2017b). Disintegration and significant dissolution of biosilica destabilise the sediment structure and lead to the collapse of intergranular matrix (Fig. 3). Elevated pressures generated during opal-A dissolution and sediment compaction, and sustained by low permeability of clay-rich overburden, drive pore water escape from the compacted opal-CT sediment (Fig. 4).

Although opal-CT cements in the sediment fabric affect the porosity (Fig. S-4f–h), their impact on pore volume decrease is subordinate to precursor opal-A dissolution (Wrona *et al.*, 2017b). This can be attributed to authigenesis of aluminosilicates, *i.e.* reverse weathering (Krissansen-Totton and Catling, 2020), which is associated with opal-CT production in deep marine deposits. These reactions compete with opal-A diagenesis for uptake of some ions, as evidenced by Si, Li, K, and Mg removal from interstitial waters in Site 794 $TZ_{A/CT}$, but Ca and Sr additions through silicate alteration (Fig. S-2). Opal-CT precipitates in the $TZ_{A/CT}$, but its solubility equilibrium is slowly reached across this boundary (Fig. 2b) likely because of the secondary clay/zeolite formation. Reverse weathering restricts massive opal-CT cementation in the anomalous compaction interval, so that the diagenetic opal sediment retains appreciable porosities (~65 % in average; Figs. 1c, 3). The retardation in silica diagenesis by secondary silicate formation is barely assisted by the precipitation of minor opaque minerals, pyrite, and gypsum (Figs. S-3a–h, S-4d).

Synthesis

In line with recent research on geochemistry of transitions from biogenic to diagenetic opal, this study developed chemical criteria for thermodynamic state of silica diagenesis at pore fluid scales. This high resolution approach relates the anomalous petrophysical shifts across the $TZ_{A/CT}$ in Site 794 to pore fluid variations of DSi and major ions, oxygen-18 composition of opal-CT, and saturation states with biogenic and diagenetic silica. Accordingly, the transformation of opal-CT from biosilica has not been fossilised since the late Miocene initiation of the

advance of petrophysical $TZ_{A/CT}$ at this site, as pore fluid advection (and diffusion) has not erased the signatures of active diagenesis. Given the implication of anomalous compaction dimensions for basin evolution future thermodynamic research may construct more inclusive pictures showing how silica diagenesis modifies the petrophysics of sediments in other basins of different thermal and geochemical histories.

Acknowledgements

This study used data derived from the ODP and IODP database and the IODP provided core samples. We would like to thank the two anonymous reviewers, whose comments greatly improved the paper, and Claudine Stirling for her work as editor.

Editor: Claudine Stirling

Additional Information

Supplementary Information accompanies this letter at https://www.geochemicalperspectivesletters.org/article2440.

Cite this letter as: Varkouhi, S., Tosca, N.J., Cartwright, J.A., Guo, Z., Kianoush, P., Jurkowska, A. (2024) Pore water chemical constraints on petrophysical shifts following biosilica diagenesis. *Geochem. Persp. Let.* 32, 39–45. https://doi.org/10.7185/geochemlet.2440

References

Damby, D.E., Llewellin, E.W., Horwell, C.J., Williamson, B.J., Najorka, J., Cressey, G., Carpenter, M.A. (2014) The α–β phase transition in volcanic cristobalite. *Journal of Applied Crystallography* 47, 1205–1215. https://doi.org/10.1107/S160057671401070X

Davies, R.J., Cartwright, J. (2002) A fossilized Opal A to Opal C/T transformation on the northeast Atlantic margin: Support for a significantly elevated palaeogeothermal gradient during the Neogene? *Basin Research* 14, 467–486. https://doi.org/10.1046/j.1365-2117.2002.00184.x

Davies, R.J., Goulty, N.R., Meadows, D. (2008) Fluid flow due to the advance of basin-scale silica reaction zones. *Geological Society of America Bulletin* 120, 195–206. https://doi.org/10.1130/b26099.1

Dixit, S., Van Cappellen, P. (2003) Predicting benthic fluxes of silicic acid from deep-sea sediments. *Journal of Geophysical Research: Oceans* 108 (C10), 3334. http://dx.doi.org/10.1029/2002JC001309

Holler, P.R. (1992) Consolidation Characteristics and Permeabilities of Sediments from the Japan Sea (Sites 798 and 799) In: Tamaki, K., Suyehiro, K., Allan, J., McWilliams, M., *et al.* (Eds.) *Proceedings of the Ocean Drilling Program. Scientific Results* 127/128 (Pt. 2). Ocean Drilling Program, College Station, Texas, 1123–1133. https://doi.org/10.2973/odp.proc.sr.127128-2.232.1992

Ibarra, D.E., Yanchilina, A.G., Lloyd, M.K., Methner, K.A., Chamberlain, C.P., Yam, R., Shemesh, A., Stolper, D.A. (2022) Triple oxygen isotope systematics of diagenetic recrystallization of diatom opal-A to opal-CT to microquartz in deep sea sediments. *Geochimica et Cosmochimica Acta* 320, 304–323. https://doi.org/10.1016/j.gca.2021.11.027

International Ocean Discovery Program (IODP) (2014) Retrieved from http://web.iodp.tamu.edu/

Kita, I., Taguchi, S., Matsubaya, O. (1985) Oxygen isotope fractionation between amorphous silica and water at 34°-93°C. *Nature* 314, 83–84. https://doi.org/10.1038/314083a0

Knauth, L.P., Epstein, S. (1976) Hydrogen and oxygen isotope ratios in nodular and bedded cherts. *Geochimica et Cosmochimica Acta* 40, 1095–1108. https://doi.org/10.1016/0016-7037(76)90051-X

Krissansen-Totton, J., Catling, D.C. (2020) A coupled carbon-silicon cycle model over Earth history: Reverse weathering as a possible explanation of a warm mid-Proterozoic climate. *Earth and Planetary Science Letters* 537, 116181. https://doi.org/10.1016/j.epsl.2020.116181

Kwon, O., Mobley, K., Carlson, R.L. (2004) Measured permeabilities of diatomaceous sediments and pelagic clay from the northwest Pacific, ODP Site 1179. In: Sager, W.W., Kanazawa, T., Escutia, C., (Eds.) *Proceedings of the Ocean Drilling Program. Scientific Results* 191. Ocean Drilling Program, College Station, Texas, 1–16. http://dx.doi.org/10.2973/odp.proc.sr.191.005.2004

Marsaglia, K.M., Milliken, K., Doran, L. (2013) Smear Slides of Marine Mud for IODP Core Description: Part I Methodology and Atlas of Siliciclastic and Volcanogenic Components. *International Ocean Discovery Program Technical Note* 1, 263p. https://doi.org/10.2204/iodp.tn.1.2013

Murata, K.J., Friedman, I., Gleason, J.D. (1977) Oxygen isotope relations between diagenetic silica minerals in Monterey Shale, Temblor Range, California. *American Journal of Science* 277, 259–272. https://doi.org/10.2475/ajs.277.3.259

Neagu, R.C., Cartwright, J., Davies, R.J., Jensen, L. (2010) Fossilisation of a silica diagenesis reaction front on the mid-Norwegian margin. *Marine and Petroleum Geology* 27, 2141–2155. http://dx.doi.org/10.1016/j.marpetgeo.2010.09.003

Pisciotto, K.A., Murray, R.W., Brumsack, H.J. (1992) Thermal History of Japan Sea Sediments from Isotopic Studies of Diagenetic Silica and Associated Pore Waters. In: Pisciotto, K.A., Ingle, J.C., Jr., von Breymann, M.T., Barron, J., *et al.* (Eds.) *Proceedings of the Ocean Drilling Program. Scientific Results* 127/128 (Pt. 1). Ocean Drilling Program, College Station, Texas, 49–56. https://doi.org/10.2973/odp.proc.sr.127128-1.113.1992

Shipboard Scientific Party (1987) Site 642: Norwegian Sea. In: Eldholm, O., Thiede, J., Taylor, E., *et al.* (Eds.) *Proceedings of the Ocean Drilling Program. Initial Reports* 104. Ocean Drilling Program, College Station, Texas, 53–453. https://doi.org/10.2973/odp.proc.ir.104.104.1987

Shipboard Scientific Party (1990) Site 794. In: Tamaki, K., Pisciotto, K., Allan, J., *et al.* (Eds.) *Proceedings of the Ocean Drilling Program. Initial Reports* 127. Ocean Drilling Program, College Station, Texas, 71–167. https://doi.org/10.2973/odp.proc.ir.127.104.1990

Shipboard Scientific Party (1994) Site 902. In: Mountain, G.S., Miller, K.G., Blum, P., *et al.* (Eds.) *Proceedings of the Ocean Drilling Program. Initial Reports* 150. Ocean Drilling Program, College Station, Texas, 63–127. https://doi.org/10.2973/odp.proc.ir.150.106.1994

Varkouhi, S., Cartwright, J.A., Tosca, N.J. (2020a) Anomalous compaction due to silica diagenesis: textural and mineralogical evidence from hemipelagic deep-sea sediments of the Japan Sea. *Marine Geology* 426, 106204. https://doi.org/10.1016/j.margeo.2020.106204

Varkouhi, S., Tosca, N.J., Cartwright, J.A. (2020b) Pore water chemistry — A proxy for tracking the signature of ongoing silica diagenesis. *Journal of Sedimentary Research* 90, 1037–1067. https://doi.org/10.2110/jsr.2020.56

Varkouhi, S., Tosca, N.J., Cartwright, J.A. (2021) Temperature-time relationships and their implications for thermal history and modelling of silica diagenesis in deep-sea sediments. *Marine Geology* 439, 106541. http://dx.doi.org/10.1016/j.margeo.2021.106541

Varkouhi, S., Cartwright, J.A., Tosca, N.J., Papineau, D. (2022) Arrested versus active silica diagenesis reaction boundaries—a review of seismic diagnostic criteria. *Basin Research* 34, 640–661. https://doi.org/10.1111/bre.12634

Volpi, V., Camerlenghi, A., Hillenbrand, C.-D., Rebesco, M., Ivaldi, R. (2003) Effects of biogenic silica on sediment compaction and slope stability on the Pacific margin of the Antarctic Peninsula. *Basin Research* 15, 339–363. https://doi.org/10.1046/j.1365-2117.2003.00210.x

von Breymann, M.T., Brumsack, H., Emeis, K.C. (1992) Depositional and diagenetic behaviour of barium in the Japan Sea. In: Pisciotto, K.A., Ingle, J.C., Jr., von Breymann, M.T., Barron, J., *et al.* (Eds.) *Proceedings of the Ocean Drilling Program. Scientific Results* 127/128 (Pt. 1). Ocean Drilling Program, College Station, Texas, 651–665. https://doi.org/10.2973/odp.proc.sr.127128-1.168.1992

Williams, L.A., Parks, G.A., Crerar, D.A. (1985) Silica diagenesis, I. Solubility controls. *Journal of Sedimentary Petrology* 55, 301–311.

Wrona, T., Jackson, C.A.-L., Huuse, M., Taylor, K.G. (2017a) Silica diagenesis in Cenozoic mudstones of the North Viking Graben: physical properties and

basin modelling. *Basin Research* 29, 556–575. https://doi.org/10.1111/bre.12168

Wrona, T., Taylor, K.G., Jackson, C.A.-L., Huuse, M., Najorka, J., Pan, I. (2017b) Impact of silica diagenesis on the porosity of fine-grained strata: an analysis of Cenozoic mudstones from the North Sea. *Geochemistry, Geophysics, Geosystems* 18, 1537–1549. https://doi.org/10.1002/2016GC006482

Yanchilina, A.G., Yam, R., Kolodny, Y., Shemesh, A. (2020) From diatom opal-A $\delta^{18}O$ to chert $\delta^{18}O$ in deep sea sediments. *Geochimica et Cosmochimica Acta* 268, 368–382. https://doi.org/10.1016/j.gca.2019.10.018

Yanchilina, A.G., Yam, R., Shemesh, A. (2021) The effect of sediment lithology on oxygen isotope composition and phase transformation of marine biogenic opal. *Chemical Geology* 570, 120175. https://doi.org/10.1016/j.chemgeo.2021.120175

Yong, Y., Lou, X., Li, S., Yang, C., Yin, X. (2014) Direct simulation of the influence of the pore structure on the diffusion process in porous media. *Computers and Mathematics with Applications* 67, 412–423, http://dx.doi.org/10.1016/j.camwa.2013.08.032

Geochemical Perspectives Letters

Pore water chemical constraints on petrophysical shifts following biosilica diagenesis

S. Varkouhi, N.J. Tosca, J.A. Cartwright, Z. Guo, P. Kianoush, A. Jurkowska

Supplementary Information

The Supplementary Information includes:

- Study Site — Geological Setting and Stratigraphy
- Sample Preparation and Analytical Methods
- Tables S-1 to S-2
- Figures S-1 to S-4
- Supplementary Information References

Study Site — Geological Setting and Stratigraphy

Ocean Drilling Program (ODP) Site 794, 40° 11.41′N and 138° 13.86′E, in the northeast of Yamato Basin of the Japan Sea is near the sudden boundary between continental crust of the Yamato Basin and oceanic crust of the Japan Basin (Fig. S-1a). Thus, while basic extrusive compositions are expected, the rock types constituting acoustic basement in the vicinity of Site 794 are diverse. Located ~50 km east of this site is the intensely tectonised zone of the Japan Sea with several thrust and reverse fault complexes of mainly steep dips (Fig. S-1b), some of which concurring with seabed sharp slopes and ridge flanks, and complex folds implicating the Cenozoic deposits (Tamaki and Honza, 1985). About 80 km west of Site 794, over the rifted continental crust near the east of Yamato Rise, normal faults involve the acoustic basement although the structure of basement in the premise of the drilled site is only slightly disrupted by faulting (Shipboard Scientific Party, 1990).

The depositional section encountered at Site 794 comprises 544 m of interbedded hemipelagic silty clay and diatomaceous clay and ooze, with lesser volumes of siliceous clay/claystone and volcanic glass and ash (Fig. 1). The sediment ranges in age from Pleistocene to middle Miocene, and the lowermost Miocene interval overlies a doleritic basement. The section is neither deformed nor disrupted by overburden removal, implying in the context of rather young age of the Yamato Basin (15 Ma; Yoon, 1997) that the back-arc setting subsided to lower–middle bathyal depths through the middle Miocene with dominant deposition of hemipelagic opal-A overburden during the early Pliocene. Mineralogical make-up, fossil content, and sedimentary structures divide the section into five major

lithostratigraphic units. The 0–293.5 m interval, with ~55 % of its total volume being biosilica (~54 % diatoms, ~1 % radiolaria, and negligible proportions of siliceous sponge spicules; Alexandrovich, 1992), consists the two upper units I and II (Fig. 1). The last occurrence of opal-A in the sediment at this site coincides with the pronounced formation of opal-CT (α-cristobalite/α-tridymite) (Varkouhi *et al.,* 2020a). This inversion from biosilica toward opal-CT occurs within an opal-A to opal-CT transition zone ($TZ_{A/CT}$) that rests at ~293.5 mbsf, coincident with the lithologic boundary between Subunits IIB and IIIA, and across which notable changes in petrophysical properties are evident (Varkouhi *et al.,* 2020b; Fig. 1). The $TZ_{A/CT}$ exhibits a stratified seismic reflector in the Yamato and northern Japan Basins and lies parallel to the present day seabed, but locally cross cuts the nearby stratal reflections (Fig. S-1c). The upper section of Unit III (Subunits IIIA) hosting the $TZ_{A/CT}$ includes ~58 m of siliceous claystone with interlayers of opal-CT porcellanite and cherts at several levels (Fig. 1). This subunit is differentiated from its overlying diatom clay by a markedly reduced biosilica content, dominant fractions of opal-CT, a denser sediment matrix, and a reduced porosity (Varkouhi *et al.,* 2020a). The highly stratified structure of the seabottom mimicking $TZ_{A/CT}$, also expressed by a corresponding variability in the compressional velocity (Fig. S-1c), indicates significant occurrences of opal-CT porcellanite and chert layers across this diagenetic reaction front (Shipboard Scientific Party, 1990).

Sample Preparation and Analytical Methods

Pore Water Geochemistry

The inorganic chemistry program at Site 794 continued its exclusive focus on analysis of 40 interstitial water samples, from a continuous section between the seabed and 524 mbsf, that were extracted from whole-round cores by Barnes water sampler (BW) and the standard ODP squeezer. The concentration of major cations Ca, K, Li, Mg, Si, Sr, and the primary indicators such as alkalinity, ammonia, chloride, pH, phosphate, salinity, sodium, and sulfate were determined during the shipboard ODP 794 (Shipboard Scientific Party, 1990). A thorough review of the sample preparation and analytical procedures for the pore water from this site is given in Murray *et al.* (1992). Variations in the interstitial water levels of silica and other major ions with burial depth, particularly the concentration gradients near and through the $TZ_{A/CT}$ build a primary source of chemical data for the present study (Fig. S-2).

The saturation index of silica polymorphs involved in biogenic silica diagenesis was assessed utilising the SpecE8 program of Geochemist's Workbench Community. The activity of aqueous silica and saturation status of silica minerals were determined using interstitial water concentrations of dissolved silicon (DSi), major ions (Mg^{2+}, Ca^{2+}, K^{+}), and primary indicators (pH, Na^{+}, Cl^{-}, SO_4^{2-}), and sediment ambient temperatures. This program benefits from the Debye-Hückel theory, which assigns an activity coefficient to each aqueous species using interstitial fluid's ionic strength. Because of the limited precision of this procedure at ionic strengths higher than 1 molal, the SpecE8 calibrates the activity on the basis of actual ionic strength values, whatever is lowest (< 0.5 molal). The program looks through archives of equilibrium constants (from 0 to 300 °C across the steam saturation chart; Bethke and Yeakel, 2016) with which the DSi activity is converted into saturation states with silica polymorphs using the equation:

$$\log (Q/K) = \log Q - \log K \qquad \text{(Eq. S-1)}$$

where Q is the activity of DSi, K the equilibrium constant, and Q/K the saturation index (Fig. 2).

Physical Property Measurements

The ODP performed an inclusive programme of petrophysical measurements on Site 794 core samples, including magnetic susceptibility, Gamma Ray Attenuation Porosity Evaluator density, and compressional wave velocity on the multi-sensor track, index properties, and thermal conductivity. A thorough review of the procedures conducted to collect, analyse, and systematise regular physical properties determinations on recovered sediment samples is given in

Blum (1997). Because of their high resolution measurement intervals (commonly 0.7–1.5 m for density stations, 1–1.5 m for porosity and velocity stations, and ~35 cm for the borehole logging tools; Varkouhi, 2018), physical property data are precise indicators for the depth to anomalous compaction near or at the top of $TZ_{A/CT}$ (*e.g.,* Neagu, 2011). The ODP conducted index properties, including wet-bulk, dry-bulk, and grain densities, porosity, and interstitial water content were utilised in this study to understand the controls on petrophysics of the sediments from Site 794 (Figs. 1–3).

Smear Slides Examination

The relative abundance of biosilica and lithogenic components of Site 794 sediments presented in this study (Figs. 1, 2) is based on the results of smear slides examinations conducted by Varkouhi (2018) and Varkouhi *et al.* (2020a) on 37 core samples provided by International Ocean Discovery Program (IODP). As the core repository was devoid of any sample left from the working-half section, no cored sediment for the first 100 m at this site was at hand for our analyses. Varkouhi (2018) outlines the details of the procedure for preparation of smear slides. During these studies, major and minor compositions of the fine-grained sediments of Site 794 and their biogenic, mineral, and lithogenic fractions were identified and described using smear slides under a polarising Leica optical microscope DM750 P. The volume percentage of these components was estimated by following the visual assessment scheme of Marsaglia *et al.* (2013). For a more accurate identification of lithogenic components as well as the quantification of biosilica, the pre-existing smear slides were further interrogated under the same microscope and photomicrographed in this study (Fig. S-3a–h).

X-ray Diffraction (XRD)

The fine powders prepared from the 37 cores and X-ray diffraction (XRD) scanned by Varkouhi (2018) and Varkouhi *et al.* (2020b) were re-estimated in this work using a PANalytical Empyrean Series 2 powder diffractometer. The methods for preparation of finely powdered samples for XRD analysis are detailed in Varkouhi (2018). The diffractometer with a cobalt source (Co-Ka) having a step rate of 0.0179/s over a 2h range from 5 to 858, housed in the Department of Earth Sciences, University of Oxford determined the abundance and relative extent of opal-CT and major crystalline components of the sediment (Table S-1). Crystalline phases in the samples were identified and quantified using the Match! 3.16 Build 288, which correlates the diffraction pattern of the sample to a reference data source to identify the phases present. The Reference Intensity Ratio (RIR) procedure, built upon scaling the diffraction data of phases in the sample to the diffraction of reference material (corundum), was applied to quantify the components with multiple phases. In this method, the normalised weights of identified phases are added up to 100 wt. % of the crystalline proportion.

Scanning Electron Microscopy (SEM)

The polished blocks formerly prepared from 6 core samples of Site 794 and analysed under scanning electron microscope (SEM) by Varkouhi (2018) and Varkouhi *et al.* (2020a, 2020b) were re-examined in this study using a FEI Quanta 650 FEG (field emission gun) SEM, hosted by the Department of Earth Sciences, University of Oxford. Procedures for preparation of resin impregnated polished blocks for SEM observations are reported in Varkouhi (2018). The SEM instrument was run in a high vacuum mode and equipped with a secondary electron detector, enabling the direct observation of the details of the sediments biosiliceous constituents. The textural features, including the presence and distribution of siliceous frustules in the sediment matrix, their dissolution and redeposition as crystalline silica polymorphs, and the fabric and pore evolution were particularly focused (Fig. S-4a–h).

$\delta^{18}O$ Stable Isotope Analysis and Isotopic Temperatures

From the total of 37 core samples, a subset of 27 representative samples with sufficient opal-CT were derived for $\delta^{18}O$ isotopic analysis. Besides diagenetic silica polymorphs (opal-CT and quartz) but minor to nil biosilica contents (Table S-1, Figs. 1, 2), these samples mostly contain clayey fragments and minor fractions of detrital quartz (Fig. S-3d–h). It

was thus imperative to isolate diagenetic silica from these samples to exclude oxygen additions from other mineral phases. This purpose was achieved by following Pisciotto *et al.* (1992) separation procedure, which has no marked effects on the isotopic extent of the isolated opal-CT and quartz, and utilises pyrosulfate fusion and acid treatments to eliminate all minerals excluding diagenetic silica, and sodium hydroxide to dissolve opal-CT from sample fractions containing both opal-CT and quartz. Because this chemical procedure cannot differentiate detrital versus diagenetic quartz, the importance of isotopic uncertainties caused by detrital quartz fractions was assessed using formerly published isotopic data from Site 794 (Pisciotto *et al.,* 1992). Combining this assessment with optical microscopic examinations by the present study, which verify fine detrital quartz scattered in the sample, and mineral composition based on XRD analysis of the bulk powdered sediment, the quartz in our interrogated samples is mainly detrital. Accordingly, the $\delta^{18}O$ values of commonly changing from +2 to +18 ‰, with a reference value of +9.36 ‰ in this range, lie within the silica realms known to largely consist of detrital quartz (Kita and Taguchi, 1986). The ^{18}O isotopic analysis of silica for this study was conducted using an isotope ratio mass spectrometers (IRMS) at Stable Isotope Lab of the Department of Earth Sciences, University of Oxford. Refer to Pisciotto (1981) and Pisciotto *et al.* (1992) for a complete review of the method used to prepare the samples for ^{18}O analysis.

Given that each analysed sample contained opal-CT and quartz, the $\delta^{18}O$ of opal-CT was calculated using the equation:

$$\delta^{18}O \text{ opal–CT} = [(\delta^{18}O \text{ opal–CT+quartz}) - (\text{wt. \% quartz} \times \delta^{18}O \text{ quartz})] \div \text{wt. \% opal–CT} \quad \text{(Eq. S-2)}$$

with a reference value of +9.36 ‰ for $\delta^{18}O$ quartz of the samples (following Kita and Taguchi, 1986). The results of $\delta^{18}O$ opal-CT analysis reported in parts per thousand (‰) are proportional to Standard Mean Ocean Water (SMOW) (Table S-2), with an average of 0.5 ‰ the contrasts among replicate analyses. The isotopic temperatures of silica formation in the sediments were calculated based on the $\delta^{18}O$ values for opal-CT using the fractionation expression of Kita *et al.* (1985) (Table S-2). This expression relates the temperatures of opal-CT formation to oxygen isotopic compositions of silica transformation using a fractionation index (α) between opal-CT and the pore water (Table S-2), which is defined as:

$$\alpha = (1 + 10^{-3}\, \delta^{18}O \text{ opal–CT}) \div (1 + 10^{-3}\, \delta^{18}O \text{ pore water}) \quad \text{(Eq. S-3)}$$

This apparent factor is smaller at lower temperatures of opal-CT precipitation (commonly below 60° C), and the smaller fractionation indices are associated with greater variations in the $\delta^{18}O$ of interstitial water (Kita and Taguchi, 1986). Because of minute isotopic depletion gradients in Site 794 (Varkouhi *et al.,* 2020b), the interstitial water from depths nearmost each opal-CT sample makes minor difference in the computed fractionation factor and opal-CT temperatures. Thus, a mean pore water $\delta^{18}O$ of -4.1 ‰ was accepted to be used in Equation S-3 by following Pisciotto *et al.* (1992).

The oxygen isotope fractionation factor of Kita *et al.* (1985) was preferred over other fractionation expressions, including those from Sharp *et al.* (2016), as it links the oxygen isotopic composition of amorphous silica to pore water within a temperature range (35.4–53.3 °C; Table S-2) comparable to that documented for the diagenetic silica conversion (Varkouhi *et al.,* 2021). The computed fractionation factors for the $TZ_{A/CT}$ frontiers (1.0325 across the $TZ_{A/CT}$ top ~293 mbsf and 1.0292 near the base at 345 mbsf, with $\delta^{18}O$ values of 28.3 and 24.8 ‰, respectively; Table S-2) match those of the moderate to high temperature (> 30°C) expression of Knauth and Epstein (1976) for ODP Site 795 neighbouring Site 794 (1.0286 at the $TZ_{A/CT}$ top 330 mbsf and 1.027 near the $TZ_{A/CT}$ base 405 mbsf; Yanchinila *et al.,* 2020). For both low (< 30 °C) and high temperatures, the fractionation factors in this study, Pisciotto *et al.* (1992), and Yanchinila *et al.* (2020) however markedly differ from those modelled by Ibarra *et al.* (2022) for Site 795 sediments using the Sharp *et al.* (2016) expression. This difference includes the $TZ_{A/CT}$ sediment isotopic temperatures,

ranging from 77 to 89 °C (Ibarra *et al.,* 2022), which are more than twice those extracted by Pisciotto *et al.* (1992) for the same sediment. This discrepancy can be related to the thermodynamic state of the $TZ_{A/CT}$ at Site 795 as the isotopic temperatures are typically lower than ambient temperatures across the anomalous compaction interval in that site, while the ancient thermal gradient (233 °C/km) is greater than the present one (132 °C/km; Varkouhi *et al.,* 2020b).

Supplementary Tables

Table S-1 Normalised crystalline contents based on X-ray diffraction analysis of bulk powdered samples in Site 794 (re-analysed and modified from Varkouhi, 2018 and Varkouhi *et al.,* 2020b). α-Crs—α-cristobalite, α-Trd—α-tridymite, An—anorthite, Phg—phengite, Qtz—quartz.

Lithologic unit **	Core, section, interval, cm	Depth, mbsf	Mineral abundance, wt. %					α-Crs, cts
			An	α-Crs	Phg	Qtz	α-Trd	
IIA	127-794A-11H-6, 37–38	100.17	28.3	2.8	29.1	35.6	4.2	402
	127-794A-17X-1, 48–49	149.98	34	5.2	21.7	35.6	3.5	379.7
	127-794A-22X-2, 113–114	200.13	34.3	1.9	24.9	33.6	5.3	472.7
IIB	127-794A-27X-3, 80–81	249.8	36.2	3.5	27.3	28.8	4.2	491.9
	127-794A-31X-4, 100–101 *	290.1	45.8	–	28.4	25.8	–	–
	127-794A-31X-5, 50–51	291.1	35.9	3.1	23.5	33.5	4	486.4
	127-794A-31X-6, 90–91	293	30.4	4.7	23	36.9	5	315
IIIA	127-794A-32X-1, 22–23	293.72	26.9	4.4	26.5	28.2	14	435.7
	127-794A-32X-1, 100–101 *	294.5	37.5	–	25.7	36.8	–	–
	127-794A-32X-2, 5–6	295.05	31	4.7	24	32	8.3	470.1
	127-794A-32X-2, 100–101 *	296	37.3	–	19.3	43.4	–	–
	127-794A-32X-3, 46–47	296.96	30.5	6	23	32.5	8	276.2
	127-794A-32X-3, 100–101 *	297.5	27.5	7	25.2	40.3	–	23
	127-794A-32X-CC, 34–35	298.45	32.3	7.7	23	28	9	263.4
	127-794A-33X-1, 0–1	303.3	1	22.9	15.5	28.6	32	10257.5
	127-794A-33X-1, 5–6	303.35	2	22.5	15.1	30.3	30.1	4257.1
	127-794A-33X-1, 10–11	303.4	1	19.1	19.3	30	30.6	4163.7
	127-794A-33X-1, 35–36	303.65	30.5	6	24	31	8.5	172.7
	127-794A-33X-1, 70–71	304	29.5	5.4	22	30.5	12.6	246
	127-794A-33X-1, 100–101 *	304.3	29	–	29.5	41.5	–	–
	127-794A-33X-1, 104–105	304.34	25.3	5.9	33.5	26.3	9	131.5
	127-794A-33X-2, 9–10	304.89	26.2	6.6	27.3	31.4	8.5	257.5
	127-794A-33X-3, 68–69	306.98	31	6.6	21	33	8.4	288.5
	127-794A-33X-4, 12–13 *	307.92	18.1	24.3	37.7	19.9	–	110
	127-794A-33X-4, 119–120	308.99	29.9	7.5	25	29.8	7.8	217
	127-794A-33X-5, 100–101 *	310.3	33.5	–	20.4	46.1	–	–
	127-794A-33X-6, 20–21	311	27	6.4	27.1	31.1	8.4	264.2
	127-794A-34X-1, 40–41	313	33	7.2	30.1	21.2	8.5	245.2
	127-794A-34X-2, 90–91	315	29	6.5	25.9	31	7.6	295.9
	127-794A-35X-1, 5–6	322.25	28.8	8	23	32	8.2	291.3
	127-794A-35X-2, 30–31	324	28	7.6	24	32	8.4	227.5
	127-794A-35X-3, 80–81	326	30.4	7.6	19.2	34.5	8.3	333.1
	127-794A-35X-4, 130–131	328	28.5	6.1	24.8	33.9	6.7	275

Table S-1 Continued.

Lithologic unit	Core, section, interval, cm	Depth, mbsf	Mineral abundance, wt. %					α-Crs, cts
			An	α-Crs	Phg	Qtz	α-Trd	
	127-794A-35X-6, 38–39	330.08	29.5	7.5	22	32.8	8.2	295
	127-794A-36X-1, 21–22	332.11	29.8	8.2	23.2	27	11.8	149.1
	127-794A-36X-2, 55–56	333.95	28.1	7.7	24.5	31	8.7	316.1
	127-794A-36X-3, 110–111	336	31	7	23.7	30.5	7.8	215.8
IIIA	127-794A-36X-5, 54–55	338.44	31.1	7.3	25.7	24.7	11.2	187.2
	127-794B-5R-1, 39–40 *	338.69	23.6	24.6	16.8	35	–	562
	127-794B-5R-1, 49–50 *	338.79	25	17.2	28.3	29.5	–	317
	127-794A-37X-1, 0–1	341.6	37.4	6	25.6	24.9	6.1	150
	127-794A-37X-2, 19–20	343.29	30.1	6.8	25.5	29.8	7.8	276.5
	127-794A-37X-3, 40–41	345	25.6	7.9	33.6	17.4	15.5	266.1
	127-794A-37X-3, 140–141	346	26.1	17.5	24.5	22.9	9	543.2
	127-794A-37X-CC, 30–31	346.63	28.7	8.8	15	23	24.5	347.5
	127-794B-6R-CC, 5–6	347.85	24.6	11.4	18.3	19.9	25.8	912.7
	127-794B-6R-CC, 7–8 *	347.87	28.9	27.1	19.2	24.8	–	620

* Relative abundance of mineral phases derived from XRD analyses performed by ODP, accessible through IODP (2014).

** Refer to Lithology column of Figure 1 for description of the stratigraphic units.

Table S-2 Opal-CT and quartz contents, normalised to 100 wt. % of the crystalline fraction, and their oxygen isotopic composition and fractionation factors between the silica precipitates and pore water (α) for samples from Sites 794. Also shown are isotopic temperatures derived based on $\delta^{18}O$ of opal-CT and the fractionation factor.

Core, section, interval, cm	Depth, mbsf	Abundance, wt. %		$\delta^{18}O$ Qtz + Opal-CT, ‰	$\delta^{18}O$ Opal-CT, ‰	α	Temperature,°C
		Opal-CT	Qtz				
127-794A-31X-5, 50–51	291.1	17.5	82.5	12.8	29.1	1.0333	41.8
127-794A-31X-6, 90–91	293	20.8	79.2	13.3	28.3	1.0325	35.4
127-794A-32X-1, 22–23	293.72	39.7	60.3	15.9	25.8	1.0300	48
127-794A-32X-2, 5–6	295.05	28.9	71.1	14.2	26	1.0302	46.8
127-794A-32X-3, 46–47	296.96	30.1	69.9	13.6	23.6	1.0278	53.1
127-794A-32X-3, 146–147 *	297.96	83.2	16.8	21.6	24.1	1.0283	56
127-794A-32X-CC, 34–35	298.45	37.4	62.6	15.1	24.8	1.0290	51
127-794A-33X-1, 0–1	303.3	65.8	34.2	20	25.5	1.0297	49.5
127-794A-33X-1, 5–6	303.35	63.5	36.5	19.7	25.6	1.0298	49.2
127-794A-33X-1, 10–11	303.4	62.4	37.6	19.5	25.6	1.0298	48.8
127-794A-33X-1, 70–71	304	37.1	62.9	15.4	25.8	1.0300	47.9
127-794A-33X-1, 104–105	304.34	36.2	63.8	15.5	26.2	1.0304	46.1
127-794A-33X-3, 68–69	306.98	31.3	68.7	14.7	26.5	1.0307	44.3
127-794A-33X-4, 119–120	308.99	33.9	66.1	15.1	26.3	1.0305	45.6
127-794A-33X-6, 20–21	311	32.3	67.7	14.9	26.4	1.0306	45.1
127-794A-34X-1, 40–41	313	42.6	57.4	16.7	26.6	1.0308	44
127-794A-34X-2, 90–91	315	31.3	68.7	14.8	26.8	1.0310	42.7
127-794A-35X-1, 5–6	322.25	33.6	66.4	15	26.1	1.0303	46.6
127-794A-35X-2, 30–31	324	33.3	66.7	14.9	26.1	1.0303	46.3
127-794A-35X-3, 80–81	326	31.6	68.4	14.7	26.4	1.0306	44.9
127-794A-35X-4, 130–131	328	27.4	72.6	14	26.3	1.0305	45.5
127-794A-35X-6, 38–39	330.08	32.4	67.6	14.7	25.9	1.0301	47.3
127-794A-36X-2, 55–56	333.95	34.6	65.4	15	25.7	1.0299	48.4
127-794A-36X-3, 110–111	336	32.7	67.3	14.6	25.3	1.0295	50.2
127-794A-36X-5, 54–55	338.44	42.8	57.2	16.5	26	1.0302	47.8
127-794A-37X-1, 54–55 *	342.14	85.1	14.9	21.7	24.4	1.0286	55.7

Table S-2 Continued.

127-794A-37X-3, 40–41	345	57.4	42.6	18.2	24.8	1.0292	53.3
127-794A-37X-3, 140–141	346	53.7	46.3	17.8	25	1.0292	52.6
127-794B-6R-CC, 5–6	347.85	65.2	34.8	19.9	25.6	1.0298	49.1
794B-7R-1, 14–15 *	356.74	84.5	15.5	23.8	25.9	1.0301	47.3
794B-9R-1, 56–57 *	376.56	77	23	23.1	25.3	1.0295	50.8
794B-10R-1, 16–17 *	385.76	88.8	11.2	26.4	27.7	1.0319	38.5

* $\delta^{18}O$ isotopic data derived from Pisciotto *et al.* (1992).

Supplementary Figures

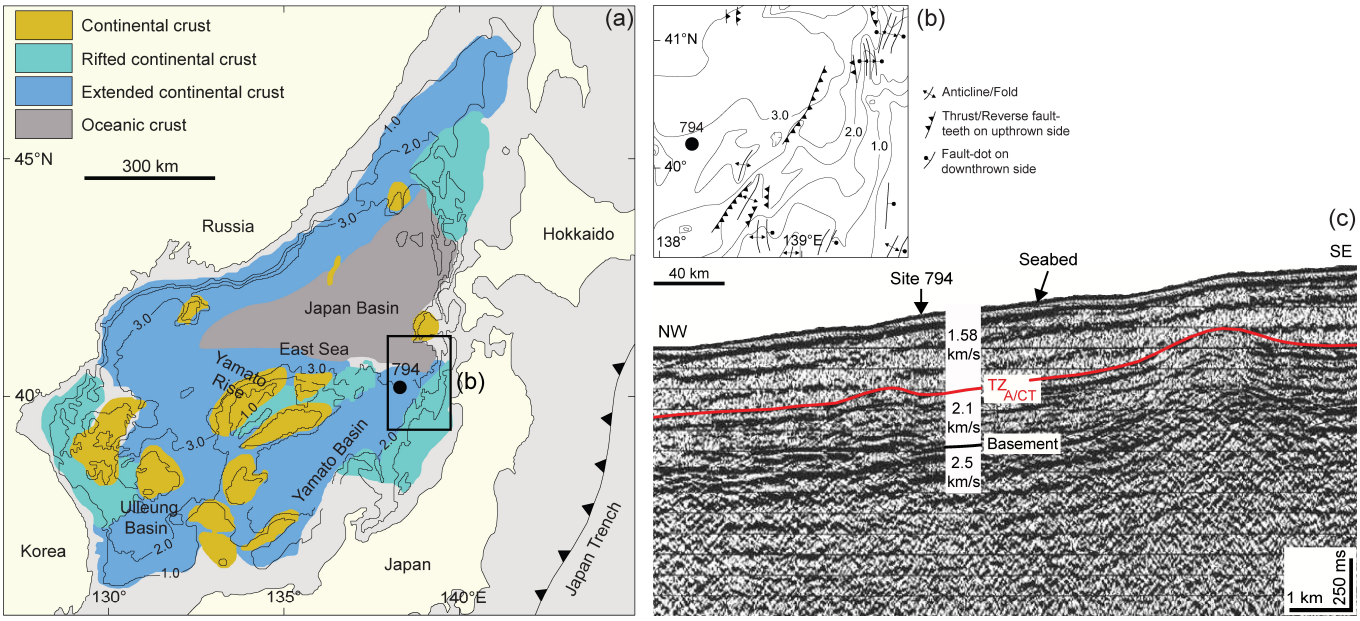

Figure S-1 Tectonic and stratigraphic setting of ODP Site 794. **(a)** Site 794 on map of the Japan Sea crustal structures (redrawn and modified from Tamaki *et al.,* 1992; Yoon *et al.,* 2014). The crust types are differentiated on the basis of seismic surveys, seafloor sampling, geomagnetism, and topographic analyses. Bathymetric contours are in kilometres. **(b)** Site 794 neighbouring highly faulted and folded eastern tectonic zone of the Japan Sea (redrawn and modified from Shipboard Scientific Party, 1990; Varkouhi *et al.,* 2020b). Bathymetric contour lines are in kilometres. **(c)** Opal-A to opal-CT transition zone on a multi-channel seismic section near Site 794 (reprinted and modified from Shipboard Scientific Party, 1990; Varkouhi *et al.,* 2020b). The $TZ_{A/CT}$ cross cuts the host strata, but simulating the modern seabottom.

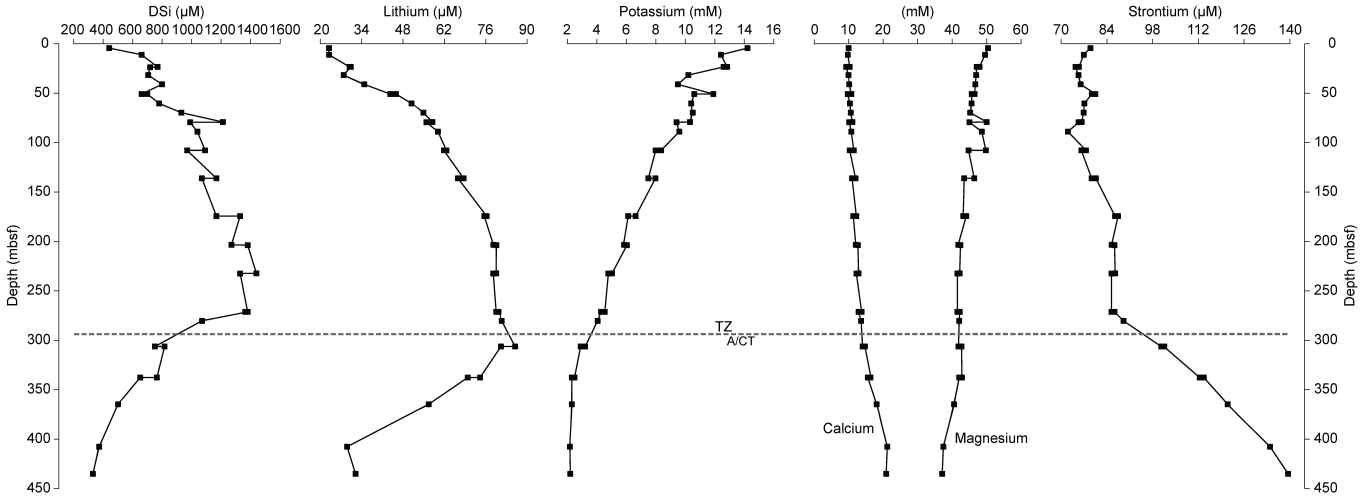

Figure S-2 Concentration–depth profiles of DSi, lithium, potassium, calcium, magnesium, and strontium at Site 794, built upon the data from IODP (2014) open access databank. Dashed line marks the top of the $TZ_{A/CT}$ at ~293.5 mbsf as determined based on abrupt petrophysical changes (Varkouhi *et al.,* 2020a, 2020b).

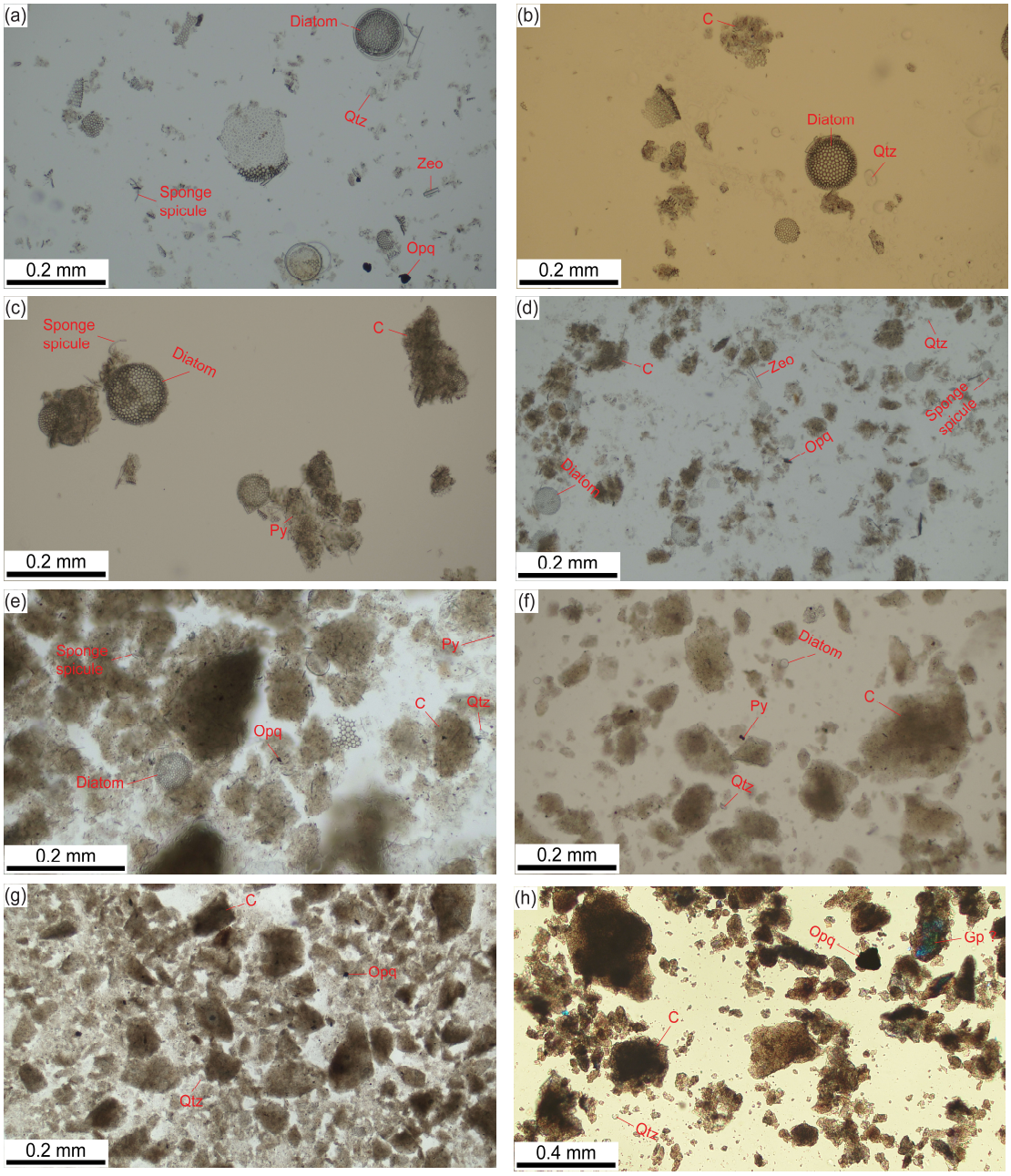

Figure S-3 Photomicrographs of siliceous sediments in Site 794. **(a)** Siliceous ooze with diatoms, low fraction of sponge spicules, and minor quartz, opaque minerals, and zeolite (Sample 127-794A-11H-6, 37–38 cm, at 100.17 mbsf). **(b)** Diatomaceous ooze containing clayey particles and low quartz content (Sample 127-794A-17X-1, 48–49 cm, at 149.98 mbsf). **(c)** Diatomaceous clay with low amount of sponge spicules and minor pyrite (Sample 127-794A-22X-2, 113–114 cm, at 200.13 mbsf). **(d)** Diatom clay containing minor fractions of sponge spicules, quartz, opaque, and zeolite (Sample 127-794A-31X-5, 50–51 cm, at 291.1 mbsf). **(e)** Silty clay with low contents of diatoms and sponge spicules and minor amounts of opaque minerals, pyrite, and quartz (Sample 127-794A-31X-6, 90–91 cm, at 293 mbsf). **(f)** Siliceous clay with minor diatoms, pyrite, and quartz (Sample 127-794A-32X-1, 22–23 cm, at 293.72 mbsf). **(g)** Siliceous claystone containing minor amounts of opaque minerals and quartz (Sample 127-794A-33X-1, 0–1 cm, at 303.3 mbsf). **(h)** Siliceous claystone with opaque minerals and low proportions of quartz and gypsum (Sample 127-794A-37X-3, 40–41 cm, at 345 mbsf). C—clay, Gp—gypsum, Opq—opaque, Py—pyrite, Zeo—zeolite.

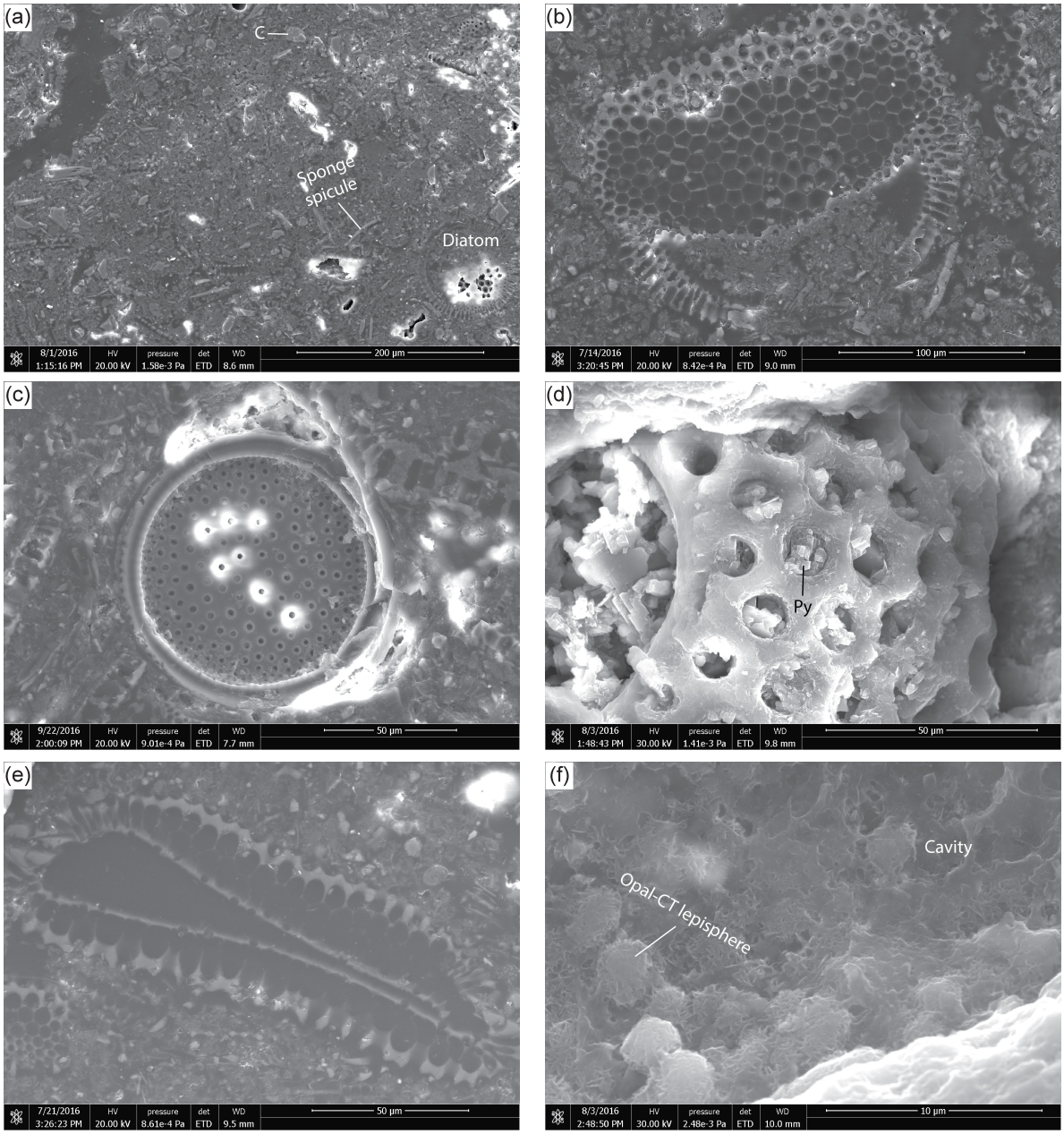

Figure S-4 Scanning electron microscope (SEM) photomicrographs of biosiliceous sediments is Site 794. **(a)** Siliceous ooze with dominant proportion of fragmented and dissolved diatom frustules, clayey particles, and low fraction of sponge spicules (Sample 127-794A-11H-6, 37–38, at 100.17 mbsf). **(b)** Deteriorated outer layer of a diatom valve, and moderate to extensive dissolution of the inner structure starting from the edge of layers (Sample 127-794A-17X-1, 48–49 cm, at 149.98 mbsf). **(c)** Rather intact structure of a diatom valve. This layer survived dissolution but the outer layers were possibly dissolved and removed (Sample 127-794A-17X-1, 48–49 cm, at 149.98 mbsf). **(d)** Authigenic cubic crystals of pyrite filling frustules of a deteriorated diatom (Sample 127-794A-22X-2, 113–114, at 200.13 mbsf). **(e)** Deterioration due to extensive dissolution of a diatom valve (Sample 127-794A-27X-3, 80–81 cm, at 249.8 mbsf). **(f)** Opal-CT lepispheres partly filling a cavity formed from biosilica dissolution (Sample 127-794A-33X-1, 0–1 cm, at 303.3 mbsf).

Figure S-4 Continued.

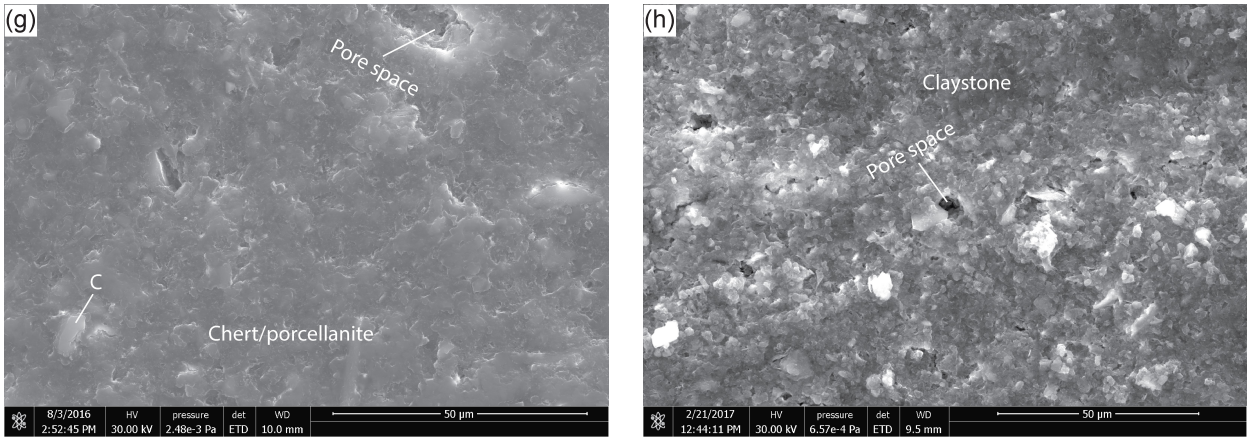

Figure S-4 Continued **(g)** Nearly homogenous dense opal-CT chert/porcellanite facies lacking biosilica (Sample 127-794A-33X-1, 0–1 cm, at 303.3 mbsf). **(h)** Dense claystone with boring-like pores scattered in the sediment matrix (Sample 127-794A-35X-1, 5–6 cm, at 322.25 mbsf).

Supplementary Information References

Alexandrovich, J.M. (1992) Radiolarians from Sites 794, 795, 796, and 797 (Japan Sea). In: Pisciotto, K.A., Ingle, J.C., Jr., von Breymann, M.T., Barron, J., *et al.* (Eds.) *Proceedings of the Ocean Drilling Program. Scientific Results* 127–128 (Pt. 1). Ocean Drilling Program, College Station, Texas, 291–307. http://dx.doi.org/10.2973/odp.proc.sr.127128-1.134.1992

Bethke, C.M., Yeakel, S. (2016) *The Geochemist's Workbench, Release 11: GWB Essentials Guide; Aqueous Solutions LLC*. Champaign, Illinois, 188 p.

Blum, P. (1997) Physical Properties Handbook: A Guide to the Shipboard Measurement of Physical Properties of Deep-sea Cores. *Ocean Drilling Program Technical Note* 26, Ocean Drilling Program, College Station, Texas. https://doi.org/10.2973/odp.tn.26.1997

Ibarra, D.E., Yanchilina, A.G., Lloyd, M.K., Methner, K.A., Chamberlain, C.P., Yam, R., Shemesh, A., Stolper, D.A. (2022) Triple oxygen isotope systematics of diagenetic recrystallization of diatom opal-A to opal-CT to microquartz in deep sea sediments. *Geochimica et Cosmochimica Acta* 320, 304–323. https://doi.org/10.1016/j.gca.2021.11.027

International Ocean Discovery Program (2014) Retrieved from http://web.iodp.tamu.edu/

Kita, I., Taguchi, S., Matsubaya, O. (1985) Oxygen isotope fractionation between amorphous silica and water at 34°-93°C. *Nature* 314, 83–84. https://doi.org/10.1038/314083a0

Kita, I., Taguchi, S. (1986) Oxygen isotopic behaviour of precipitating silica from geothermal water. *Geochemical Journal* 20, 153–157. https://doi.org/10.2343/geochemj.20.153

Knauth, L.P., Epstein, S. (1976) Hydrogen and oxygen isotope ratios in nodular and bedded cherts. *Geochimica et Cosmochimica Acta* 40, 1095–1108. https://doi.org/10.1016/0016-7037(76)90051-X

Marsaglia, K.M., Milliken, K., Doran, L. (2013) Smear Slides of Marine Mud for IODP Core Description: Part I Methodology and Atlas of Siliciclastic and Volcanogenic Components. *International Ocean Discovery Program Technical Note* 1, 263 p. https://doi.org/10.2204/iodp.tn.1.2013

Murray, R.W., Buchholtz ten Brink, M.R., Brumsack, H.-J., Gerlach, D.C., Russ, G.P., III. (1992) Rare Earth, Major, and Trace Element Composition of Leg 127 Sediments. In: Pisciotto, K.A., Ingle, J.C., Jr., von Breymann, M.T., Barron, J., *et al.* (Eds.) *Proceeding of the Ocean Drilling Program*. *Scientific Results* 127–128 (Pt. 1). Ocean Drilling Program, College Station, Texas, 677–695. http://dx.doi.org/10.2973/odp.proc.sr.127128-1.176.1992

Neagu, R.C. (2011) The Relationship between Biogenic Silica Diagenesis and the Physical Properties of Sediments Studied Using Seismic and Well Data. PhD Thesis. Cardiff University, 275 p.

Pisciotto, K.A. (1981) Diagenetic trends in the siliceous facies of the Monterey Shale in the Santa Maria region, California. *Sedimentology* 28, 547–571. https://doi.org/10.1111/j.1365-3091.1981.tb01701.x

Pisciotto, K.A., Murray, R.W., Brumsack, H.J. (1992) Thermal History of Japan Sea Sediments from Isotopic Studies of Diagenetic Silica and Associated Pore Waters. In: Pisciotto, K.A., Ingle, J.C., Jr., von Breymann, M.T., Barron, J., *et al.* (Eds.) *Proceedings of the Ocean Drilling Program. Scientific Results* 127–128 (Pt. 1). Ocean Drilling Program, College Station, Texas, 49–56. https://doi.org/10.2973/odp.proc.sr.127128-1.113.1992

Sharp, Z.D., Gibbons, J.A., Maltsev, O., Atudorei, V., Pack, A., Sengupta, S., Shock, E.L., Knauth, L.P. (2016) A calibration of the triple oxygen isotope fractionation in the SiO_2–H_2O system and applications to natural samples. *Geochimica et Cosmochimica Acta* 186, 105–119, https://doi.org/10.1016/j.gca.2016.04.047

Shipboard Scientific Party (1990) Site 794. In: Tamaki, K., Pisciotto, K., Allan, J., *et al.* (Eds.) *Proceedings of the Ocean Drilling Program. Initial Reports* 127. Ocean Drilling Program, College Station, Texas, 71–167. https://doi.org/10.2973/odp.proc.ir.127.104.1990

Tamaki, K., Honza, E. (1985) Incipient subduction and obduction along the eastern margin of the Japan Sea. *Tectonophysics* 119, 381–406. https://doi.org/10.1016/0040-1951(85)90047-2

Tamaki, K., Suyehiro, K., Allan, J., Ingle Jr., J.C., Pisciotto, K.A. (1992) Tectonic Synthesis and Implications of Japan Sea ODP Drilling. In: Tamaki, K., Suyehiro, K., Allan, J., McWilliams, M., *et al.* (Eds.) *Proceedings of the Ocean Drilling Program. Scientific Results* 127/128 (Pt. 2). Ocean Drilling Program, College Station, Texas, 1333–1348. http://dx.doi.org/10.2973/odp.proc.sr.127128-2.240.1992

Varkouhi, S. (2018) Biogenic Silica Diagenesis under Early Burial in Hemipelagic Marine Sediments. DPhil Thesis. University of Oxford, 428 p.

Varkouhi, S., Cartwright, J.A., Tosca, N.J. (2020a) Anomalous compaction due to silica diagenesis: textural and mineralogical evidence from hemipelagic deep-sea sediments of the Japan Sea. *Marine Geology* 426, 106204. https://doi.org/10.1016/j.margeo.2020.106204

Varkouhi, S., Tosca, N.J., Cartwright, J.A. (2020b) Pore water chemistry — A proxy for tracking the signature of ongoing silica diagenesis. *Journal of Sedimentary Research* 90, 1037–1067. https://doi.org/10.2110/jsr.2020.56

Varkouhi, S., Tosca, N.J., Cartwright, J.A. (2021) Temperature–time relationships and their implications for thermal history and modelling of silica diagenesis in deep-sea sediments. *Marine Geology* 439, 106541. http://dx.doi.org/10.1016/j.margeo.2021.106541

Yanchilina, A.G., Yam, R., Kolodny, Y., Shemesh, A. (2020) From diatom opal-A $\delta^{18}O$ to chert $\delta^{18}O$ in deep sea sediments. *Geochimica et Cosmochimica Acta* 268, 368–382. https://doi.org/10.1016/j.gca.2019.10.018

Yoon, S. (1997) Miocene–Pleistocene volcanism and tectonics in southern Korea and their relationship to the opening of the Japan Sea. *Tectonophysics* 281, 53–70. https://doi.org/10.1016/S0040-1951(97)00158-3

Yoon, S.H., Sohn, Y.K., Choughc, S.K. (2014) Tectonic, sedimentary, and volcanic evolution of a back-arc basin in the East Sea (Sea of Japan). *Marine Geology* 352, 70–88. http://dx.doi.org/10.1016/j.margeo.2014.03.004